JOURNAL OF CATALYSIS 89, 303–313 (1984)

Preparation and Characterization of Magnetite Surfaces on Metallic Iron Substrates

TERRENCE J. UDOVIC[1] AND J. A. DUMESIC[2]

Department of Chemical Engineering, University of Wisconsin, Madison, Wisconsin 53706

Received November 18, 1983; revised April 24, 1984

Magnetite (Fe_3O_4) surfaces were created on polycrystalline metallic Fe substrates by low-pressure oxidation (3×10^{-4} Pa O_2, 673 K). Conversion electron Mössbauer spectroscopy, X-ray photoelectron spectroscopy, and Auger electron spectroscopy were utilized in the characterization of these surfaces. The iron oxide overlayers were identified as magnetite using the former technique, while the latter two techniques revealed that vacuum-annealing at various temperatures below ca. 675 K was an effective means of altering the surface oxidation state. Both the degree of surface reduction and the surface cation concentration increased as the vacuum-annealing temperature was increased. In particular, as the vacuum-annealing temperature was increased from 300 to 675 K, the surface changed from an Fe_3O_4-like appearance to an FeO-like appearance. This FeO-like surface was maintained at vacuum-annealing temperatures above 675 K.

INTRODUCTION

The nature of surface sites on metal oxides is of importance for such catalytic reactions as water-gas shift, partial oxidation of hydrocarbons, and catalytic cracking. Typically, these sites are described in terms of acid/base properties. Coordinatively unsaturated metal cations may function as Lewis acids, surface oxygen anions may act as Lewis bases, and surface protons may be Brønsted acid sites. In addition, the relative surface concentrations of these various types of sites may be a function of sample pretreatment. This is especially true for reducible oxides, where the stoichiometry of the oxide is variable. In short, fundamental studies are required on "model oxide surfaces" to probe systematically the role of the surface chemical state (e.g., oxidation state) in determining the adsorptive and catalytic properties of these materials.

The present two-part study addresses the relationship between the surface oxidation state and the adsorptive properties of magnetite (Fe_3O_4). This iron oxide is in an intermediate oxidation state (between Fe_2O_3 and FeO), suggesting that the surface oxidation state may be particularly sensitive to pretreatment effects. In addition, magnetite-based catalysts are used for water-gas shift and oxidative dehydrogenation reactions. The focus of the present paper is on the preparation and characterization of magnetite surfaces. These surfaces were prepared by the controlled oxidation of metallic iron substrates, and the techniques used for sample characterization were conversion electron Mössbauer spectroscopy (CEMS), X-ray photoelectron spectroscopy (XPS), and Auger electron spectroscopy (AES). A subsequent paper (*1*) will deal with the adsorptive properties of these magnetite surfaces, as studied by temperature-programmed desorption.

RATIONALE FOR PREPARING MAGNETITE OVERLAYERS ON IRON

Structure of Oxidized Layers on Iron

Numerous iron oxidation studies have been undertaken to ascertain the corrosion

[1] Present address: U.S. Department of Commerce, National Bureau of Standards, Surface Science Division, Washington, D.C. 20234.

[2] Author to whom correspondence should be addressed.

0021-9517/84 $3.00

processes involved (e.g., (*2–15*)). These studies are complicated by the fact that more than one stable iron oxide phase can exist. In reality, the iron oxide layer usually consists of several layers of different oxide phases (stacked in the order $Fe/Fe_{1-x}O/Fe_3O_4/\gamma$-$Fe_2O3/\alpha$-$Fe_2O_3$) in various proportions (*16*).

Single-crystal iron oxidation studies (*6, 11–15*) have established that at low oxygen exposure (<ca. 100 L), the initial stages of oxidation involve dissociative chemisorption of oxygen followed by either FeO-like or spinel-like oxide formation, depending on the orientation of the iron surface. Independent of the particular surface orientation, further stages of iron oxidation result in an increase in the oxide film thickness and the layered epitaxial appearance of other oxide phases. Epitaxy between the cubic oxide phases ($Fe_{1-x}O$, Fe_3O_4, and γ-Fe_2O_3) is facilitated by the similarity in lattice structures. All three cubic oxides have the same fcc oxygen lattice structure and differ crystallographically only in the number and position of Fe cations among the interstitial sites. It appears that transitions between these three oxide phases can proceed topotaxially (*16, 17*) involving only a depletion or gain of Fe cations in the interstitial sites of the oxygen lattice. The oxidation scheme $Fe_{1-x}O \rightarrow Fe_3O_4 \rightarrow \gamma$-$Fe_2O_3$ can thus be imagined to proceed by the addition of new layers of close-packed oxygen atoms on the $Fe_{1-x}O$ lattice surface with topotaxial migration of Fe cations into this extended lattice array from the subsurface region. As a result, the subsurface Fe cation concentration would decrease with a gradual and continuous subsurface phase change from $Fe_{1-x}O$ to the spinel oxides.

According to Columbo *et al.* (*18, 19*), the formation of α-Fe_2O_3 by further oxidation of Fe_3O_4 occurs via an epitaxial, autocatalytic growth process originating at nucleation sites which consist of stacking faults in the spinel lattice. Annealing the Fe_3O_4 phase decreases the concentration of stacking faults and, subsequently, the formation rate of α-Fe_2O_3 relative to that of $Fe_{3-z}O_4$ (where $0 \leq z \leq 1$ corresponds to the cubic transition from Fe_3O_4 to γ-Fe_2O_3). Ideally, a Fe_3O_4 phase free of stacking faults will oxidize topotaxially to $Fe_{3-z}O_4$, maintaining a cubic structure.

In summary, the oxidation of iron involves both epitaxial and topotaxial growth processes. For $Fe_{1-x}O$, cationic diffusion via cation vacancies predominates due to the unusually high concentration of vacancy defects present (*20, 21*). For α-Fe_2O_3, cationic diffusion is relatively low compared to $Fe_{1-x}O$, and anionic diffusion predominates (*5, 22*). For cubic phases between these two extremes, both cationic and anionic diffusion occur, although cationic diffusion predominates (*5*).

The composition and thickness of the oxide layer is dependent on the total oxygen pressure, the oxidation temperature, the oxidation time period, and the nature (e.g., crystallographic orientation, grain size, and purity) of the iron substrate (*6*). Graham and Cohen (*8*) studied the effect of oxygen pressure (10^{-4} Pa–8 kPa) on the oxidation of polycrystalline iron foils at 623 and 673 K. It was proposed, consistent with the work of others (*6, 10*), that Fe_3O_4 formed initially on the surface and the oxide layer grew topotaxially as Fe cations diffused outward through cation vacancies in the oxide. Increasing the oxygen pressure increased the concentration of cation vacancies, thereby increasing the cation flux and the oxidation rate. The oxidation rate decreased when a continuous α-Fe_2O_3 overlayer was formed on the surface. This reduced the effective oxygen pressure at the outer surface of the Fe_3O_4 layer. At this stage, the rate-controlling step became the diffusion of oxygen inward through the α-Fe_2O_3 layer. The kinetic stability of the α-Fe_2O_3 overlayer depends on a balance between its reduction to Fe_3O_4 by diffusing Fe cations and the oxidation of Fe_3O_4 to α-Fe_2O_3 by oxygen (*10*). For example (*8*), at ca. 10^{-3} Pa, the fast diffusion of cations through Fe_3O_4 at 673 K led to continuous

reduction of any α-Fe_2O_3 to Fe_3O_4, while at 623 K the slower cation flux allowed the formation of a continuous layer of α-Fe_2O_3. At oxygen pressures less than 10^{-3} Pa, only Fe_3O_4 was observed at 623 K.

It should be noted that the above growth mechanism also applies to oxide layers formed at temperatures greater than 840 K where $Fe_{1-x}O$ is the predominant phase (*2, 23*) and below 520 K where the formation of γ-Fe_2O_3 becomes increasingly important (*5, 24*).

Finally, at the temperatures (ca. 600 K) employed to form magnetite surface layers, the oxidation rate follows the parabolic rate law developed by Wagner (*25*).

Low-Pressure Stability of the Oxidized Layers

The effects of ultrahigh vacuum (UHV) annealing on oxide overlayers grown on iron have been documented in the literature (*3, 4, 7, 9, 26, 27*). Davies *et al.* (*3*) found that, for films of α-Fe_2O_3 on top of Fe_3O_4, vacuum annealing ($<10^{-4}$ Pa) at temperatures as low as 523 K reduced the surface α-Fe_2O_3 layer to Fe_3O_4. This reduction is believed to be controlled by cation transport across the magnetite layer (*9*). At higher temperatures (ca. 1073 K), both α-Fe_2O_3 and Fe_3O_4 reduce to $Fe_{1-x}O$ (*27*).

Reduction of iron oxides under vacuum is not restricted to oxide films grown on iron. Rather, there is evidence that bulk α-Fe_2O_3 powder undergoes a partial reduction to Fe_3O_4 during vacuum annealing (*26, 28, 29*). Removal of oxygen from the lattice to the gas phase must occur to explain the observed behavior. From the nitric oxide adsorption behavior of vacuum-annealed magnetite powders, Lund *et al.* (*30*) have inferred that long vacuum treatments (14 h) at 650 K can result in the removal of as much as a monolayer of oxygen and the reduction of all surface Fe^{3+} cations to Fe^{2+} cations. In short, it appears that the surface structure of the cubic iron oxides (e.g., ratios of Fe^{3+}/Fe^{2+} cations and tetrahedral/octahedral site cations) depends on both the temperature and time of vacuum treatment.

EXPERIMENTAL

Experiments were performed utilizing conversion electron Mössbauer spectroscopy (CEMS) to study the low-pressure oxidation behavior of polycrystalline iron films. Approximately 20 nm (as estimated by a quartz-crystal thickness monitor) of ca. 90% ^{57}Fe-enriched iron (New England Nuclear) was deposited onto one face of a degreased 310 stainless-steel foil (50 × 50 × 0.025 mm, New England Nuclear). This was accomplished by vacuum evaporation from an alumina-coated Mo dimple-boat. Subsequently, the iron film was reduced in hydrogen (10^2 kPa, 623 K, 24 h). CEMS experiments were performed in the spectrometer described by Tatarchuk and Dumesic (*31*). The sample was mounted in the spectrometer on a Ti holder, exposing a 37-mm-diameter area to the 50-mCi ^{57}Co/Pd Mössbauer source. The emitted electron signal was detected by a continuous dynode electron multiplier ("Spiraltron" Galileo Electro-Optics Corp.) at a 4.2-kV multiplier voltage (gain $> 10^6$). All scans were taken at a base pressure of ca. 10^{-5} Pa. Each Mössbauer spectrum was computer-fitted using the program MFIT (*32*). The single peak near the center of each spectrum due to ^{57}Fe in both the underlying stainless-steel substrate and the surrounding stainless-steel vacuum chamber was computer-subtracted. The spectrometer was calibrated using a metallic iron foil enriched in ^{57}Fe. All isomer shifts were determined relative to this standard.

XPS and AES were employed for the characterization of the iron oxide surfaces. The polycrystalline iron foil substrates utilized in these experiments were obtained from the Materials Research Corporation (10 × 10 × 0.025 mm, MARZ grade, 99.99% purity). XPS and AES experiments were performed in a Physical Electronics Model 548 ESCA/Auger electron spectrometer pumped by a 200-liters s^{-1} ion

pump and a titanium sublimation pump. Background pressures in the analysis chamber were ca. 10^{-7} Pa. X-Ray excitation was accomplished using a magnesium source anode. The chamber was equipped with an argon-ion gun for sputtering. Degreased samples were loaded through a turbo-pumped introduction chamber and heated in the analysis chamber on the introduction rod with the aid of a pancake heater. All XPS binding energies were determined from spectral peak maxima before baseline corrections and were referenced to a carbon impurity C_{1s} binding energy of 285.0 eV (*27*). The photoelectron intensities were determined from peak areas employing two different baseline correction schemes: Scheme A, the convenient yet physically inappropriate linear baseline approximation (*33*); and Scheme B, a baseline correction function suggested by Barrie and Street (*34*), which more appropriately models the spectral peak contribution to the inelastic electron background. Iron/oxygen and iron/carbon surface atomic ratios were calculated utilizing the relative Fe_{2p}, O_{1s}, and C_{1s} sensitivity values (of 3.8, 0.63, and 1.0, respectively) from Wagner *et al.* (*35*). Ferrous/ferric surface cation ratios were estimated by computer-fitting the Fe_{2p} spectra with the Fe^{2+} and Fe^{3+} reference spectra generated from highly reduced (Fe^{2+}-enriched) and highly oxidized (Fe^{3+}-enriched) surfaces, respectively. These spectra will be shown in the next section.

Argon (99.9995%) and 85:15 CO_2/CO (99.5% pure) were obtained from Matheson. Hydrogen (99.9%) and O_2 (99.9%) were obtained from Chemetron. All gases were used without further purification.

RESULTS AND DISCUSSION

Figure 1 and Table 1 summarize the CEMS results. The initial spectrum after reduction with hydrogen was characteristic of a metallic iron film with partial alignment of the magnetic domains in the plane of the film (as evidenced by the relative magnitudes of the sextuplet line intensities (*9*)).

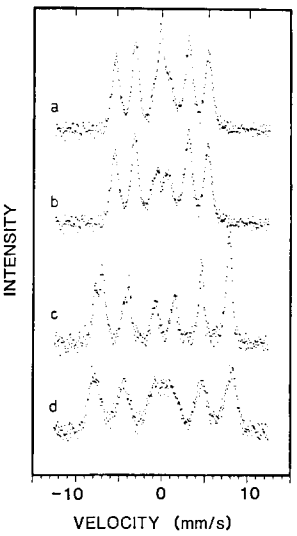

FIG. 1. Conversion electron Mössbauer spectra of ^{57}Fe on stainless steel after the following treatments: (a) 10^2 kPa H_2, 623 K, 24 h (spectrum without subtraction of stainless-steel peak near zero velocity); (b) same as spectrum (a) with subtraction of stainless-steel peak near zero velocity; (c) 2×10^{-3} Pa CO_2/CO (85 : 15), 673 K, 1 h; (d) 10^2 kPa air, 473 K, 34 h.

Upon treatment in oxygen (2×10^{-3} Pa, 673 K, 1 h), the resulting spectrum matched that of Fe_3O_4. This is evidenced in Fig. 1c by an increase in the separation between the peaks, compared to the case of metallic iron, and by the splitting of the most-negative peak into two distinct peaks. This splitting is due to different Mössbauer parameters for iron cations in octahedral and

TABLE 1

Summary of Conversion Electron Mössbauer Spectroscopy Results following Sequential Treatments

Sequential treatment	Resulting spectrum (in Fig. 1)	Oxide phase
(1) 10^2 kPa H_2, 623 K, 24 h	(b)	Fe^0
(2) 2×10^{-3} Pa O_2, 673 K, 1 h	(c)	Fe_3O_4
(3) 2×10^{-3} Pa (85 : 15) CO_2/CO, 673 K, 1 h	Same as (c)	Fe_3O_4
(4) 2×10^{-3} Pa O_2, 673 K, 6 h	Same as (c)	Fe_3O_4
(5) 10^2 kPa air, 473 K, 34 h	(d)	γ-Fe_2O_3
(6) 2×10^{-3} Pa (85 : 15) CO_2/CO, 673 K, 2 h	Same as (c)	Fe_3O_4

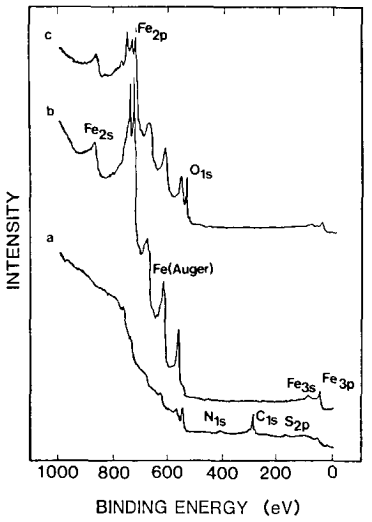

FIG. 2. X-Ray photoelectron spectra of iron surface following various treatments. (a) iron surface before treatment, (b) iron surface after sputter–anneal cleaning procedure, (c) magnetite surface after standard oxidation treatment of "clean" iron surface.

tetrahedral sites in Fe_3O_4. Further treatment in both CO_2/CO (85 : 15 molar ratio, 2 $\times$ 10^{-3} Pa, 673 K, 1 h) and oxygen (2 $\times$ 10^{-3} Pa, 673 K, 6 h) produced no additional changes in the Fe_3O_4 spectrum. γ-Fe_2O_3 was formed after heating in air (10^2 kPa, 473 K, 34 h), as seen in Fig. 1d by the fact that the splitting of the most-negative peak has disappeared. Subsequent treatment in CO_2/CO (85 : 15, 2 $\times$ 10^{-3} Pa, 673 K, 2 h) reverted the film to Fe_3O_4. In short, the results of these experiments confirmed that low-pressure oxidation of iron at ca. 673 K yields a magnetite overlayer. In addition, low-pressure (85 : 15) CO_2/CO has the ability to reduce highly oxidized surface layers to Fe_3O_4. This CO_2/CO treatment was analogous to the high-pressure treatment performed on magnetite powder catalysts by Kubsh and Dumesic (*36*).

Experiments using XPS were next performed to establish a procedure for creating "clean" iron surfaces as precursors for the synthesis of magnetite surfaces. The procedure chosen was based on the cleaning methods developed by other researchers (*37–39*). Figure 2 summarizes the experimental results. The initial XPS spectrum (Fig. 2a) of the degreased Fe foil showed the presence of an iron oxide surface layer contaminated with carbon, nitrogen, and sulfur. Argon-ion sputtering (2 kV, 15 min) at room temperature removed this oxide layer with only a moderate decrease in surface impurities. The sample was then annealed at 870 K for 1 h to reduce the amount of dissolved nitrogen. After cooling to 300 K, the sample was subjected to a series of sputter–anneal cycles (sputter, 2 kV, 5 min; anneal, 770 K, 30 min). After about five cycles, only a slight surface carbon impurity was detectable (Fig. 2b). From high–resolution spectral area analysis of the Fe_{2p} and C_{1s} peaks, the surface carbon concentration was estimated to be less than ca. 2% of a monolayer. Subsequent low-pressure oxidation (3 $\times$ 10^{-4} Pa O_2, 673 K, 45 min) formed a "clean" magnetite overlayer (Fig. 2c). This 45-min oxidation treatment was chosen as the initial oxidation treatment for the creation of the magnetite overlayer.

To estimate the thickness of the magnetite layer produced by the standard oxidation treatment, a simple optical method was employed which correlates the oxide overlayer thickness with the overlayer tarnish color. Over the 45-min oxidation, the tarnish color changed in the following sequence: metallic $\rightarrow$ golden brown $\rightarrow$ red $\rightarrow$ purple $\rightarrow$ blue. Ideally, the tarnish color is governed by the wavelength of light that undergoes destructive interference upon reflection from both the oxide surface and the underlying metal–metal oxide interface (*40*). In practice, the overlayer thickness for a given tarnish color must be empirically calibrated. Davies *et al.* (*3*) have done this for iron oxide overlayers on iron. Their results, used in conjunction with the experimentally determined color transformations during the oxidation treatment of the present study, indicated that the final overlayer was ca. 30-nm thick.

The above magnetite overlayer thickness

is in agreement with oxidation rate calculations and depth-profiling experiments using the argon-ion sputtering gun. Assuming linear-oxidation-rate behavior (i.e., the oxidation rate is limited by the oxygen impingement rate on the oxide surface) and utilizing an oxygen sticking probability of 0.025 at 673 K (*8*), the overlayer thickness can be estimated to be ca. 20 nm after the oxidation treatment (*41*). The linear-rate behavior, which had been found by Graham and Cohen (*8*), was verified by Ar-ion sputtering through oxide overlayers of different thicknesses (i.e., different oxidation times) and noting the constant change in required sputtering time with respect to change in total oxidation time.

The resultant overlayer was found to be stable under the experimental conditions of interest as evidenced by the lack of flaking and the invariance of the blue tarnish color. The results of temperature-programmed desorption studies (*1*) also indicated the absence of metallic iron on the surface following the above oxidation treatment or after any of the vacuum-annealing treatments described below.

To vary systematically the surface oxidation state of the magnetite overlayer, a standard procedure was adopted. Typically the clean oxide overlayer was (1) exposed to 1×10^{-4} Pa O_2 at 300 K, (2) increased in temperature to 950 K to desorb any admolecules accumulated from the background pressure, (3) lowered in temperature to 800 K and held for 3 min to build up the oxide overlayer, (4) lowered (or raised) to the desired treatment temperature T and held for 3 min to further oxidize the surface, and (5) vacuum-annealed at temperature T for 1.5 min (by evacuating the O_2 from the UHV chamber) to reduce the surface to a steady state condition. This type of model surface was designated by the temperature T of steps (4) and (5).

XPS experiments were performed to study the surface behavior of the magnetite overlayer as a function of pretreatment conditions. The Fe_{2p} and O_{1s} photoelectron peaks were monitored for various surfaces ranging from a 300 K surface to an 875 K surface; a fully oxidized surface (all Fe^{3+}) resulting from exposure to high-pressure (10^2 kPa) air at 300 K; and a highly reduced surface (all Fe^{2+}) created by vacuum-annealing an oxidized surface at 875 K followed by several minutes of 2-kV argon-ion sputtering. Particular features were followed as a function of surface pretreatment: the Fe_{2p} and O_{1s} binding energies as well as the Fe_{2p}/O_{1s} and $Fe^{2+}_{2p}/Fe^{3+}_{2p}$ photoelectron intensity ratios. The results are displayed in Figs. 3 and 4 and in Table 2.

The Fe_{2p} spectrum for the fully oxidized surface (Fig. 3a) is essentially an Fe^{3+} spectrum from a γ-Fe_2O_3 (or α-Fe_2O_3) surface, as evidenced by the 710.5-eV binding energy for $Fe_{2p_{3/2}}$ and the satellite structure at ca. 719 eV (*27*, *42*). The O_{1s} spectrum for this surface (Fig. 4a) indicates hydroxylation as evidenced by the high binding energy shoulder ca. 2 eV above the main peak. This is to be expected since air-exposed magnetite surfaces readily chemisorb water (*43*). The Fe_{2p} spectrum for the

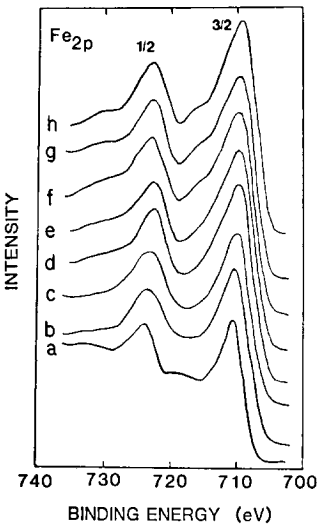

FIG. 3. Fe_{2p} X-ray photoelectron spectra for magnetite surfaces subjected to different treatments: (a) fully oxidized surface, (b) 300 K surface, (c) 440 K surface, (d) 575 K surface, (e) 675 K surface, (f) 775 K surface, (g) 875 surface, and (h) sputtered surface.

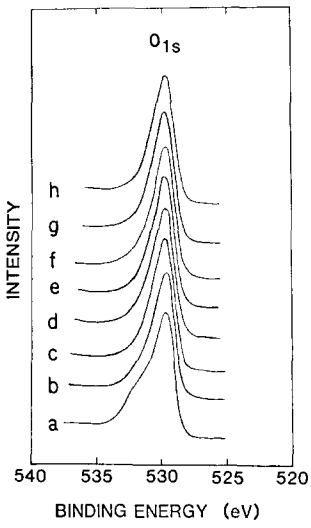

FIG. 4. O_{1s} X-ray photoelectron spectra for magnetite surfaces subjected to different treatments: (a) fully oxidized surface, (b) 300 K surface, (c) 440 K surface, (d) 575 K surface, (e) 675 K surface, (f) 775 K surface, (g) 875 K surface, and (h) sputtered surface.

highly reduced surface (Fig. 3h) is essentially an Fe^{2+} spectrum, as evidenced by the 709.3-eV binding energy for $Fe_{2p_{3/2}}$ and the satellite structure at ca. 715 eV (*27, 42*). Although the above absolute binding energies are not in exact agreement with the referenced values (*27, 42*), the 1.2-eV difference between the $Fe_{2p_{3/2}}$ binding energies for Fe^{2+} and Fe^{3+} and the satellite structure are in excellent agreement with the literature. Differences in absolute binding energies could be corrected by shifting the reference level.

The previous two surfaces were created as reference surfaces for Fe^{2+} and Fe^{3+} XPS spectra. The Fe_{2p} spectra from these two reference surfaces were combined by computer in appropriate ratios so as to give a satisfactory fit to the Fe_{2p} spectra of the other pretreated surfaces (Figs. 3b–g). Resulting Fe^{2+}/Fe^{3+} ratios are only estimations and are to be used in a qualitative sense.

The results in Table 2 illustrate the relative oxidation state of the various pretreated magnetite surfaces. The 875 to 675 K surfaces are reduced (mainly Fe^{2+}) surfaces with high surface cation concentrations, as evidenced by the relatively high Fe^{2+}/Fe^{3+} and Fe/O atomic ratios and the low $Fe_{2p_{3/2}}$ binding energy (709.6 eV). Decreasing the pretreatment temperature below 575 K results in an increase in the surface oxidation state (i.e., decreases in the Fe^{2+}/Fe^{3+} ratio and $Fe_{2p_{3/2}}$ binding energy) and a decrease in surface cation concentration (i.e., a decrease in the Fe/O atomic ratio). These oxidation state trends are apparent from the Fe_{2p} XPS spectra in Fig. 3, which illustrates the changing spectral contributions from Fe^{2+} and Fe^{3+} satellite

TABLE 2

Summary of X-Ray Photoelectron Spectroscopy Results for Magnetite Surfaces Subjected to Various Treatments (Figs. 3 and 4)

Type of surface	Binding energy, E_B (eV)			Fe/O atomic ratio		Fe^{2+}/Fe^{3+} Ratio
	$Fe_{2p_{1/2}}$	$Fe_{2p_{3/2}}$	O_{1s}	Scheme A	Scheme B	
(a) Oxidized	723.6	710.5	529.8	0.45	0.41	0
(b) 300 K	723.4	710.3	529.8	0.78	0.71	~0.7
(c) 440 K	723.0	710.1	529.7	0.83	0.75	~1.5
(d) 575 K	722.5	709.7	529.7	0.89	0.80	~2
(e) 675 K	722.4	709.6	529.7	0.89	0.80	~5
(f) 775 K	722.4	709.6	529.7	0.89	0.80	~10
(g) 875 K	722.4	709.6	529.7	0.89	0.80	~10
(h) Sputtered	722.1	709.3	529.7	1.1	0.99	∞

structure as well as the shifts in Fe_{2p} binding energy for the pretreated surfaces below the 675 K surface.

The O_{1s} XPS spectra in Fig. 4 are essentially constant except for the hydroxyl feature from the fully oxidized surface (Fig. 4a). The spectra display a constant O_{1s} binding energy of 529.7 eV and a slightly asymmetric peak tailing toward the high-binding-energy side. As mentioned above, this high-binding-energy contribution is probably due to the presence of oxygen in a hydroxyl state and/or as nonstoichiometric surface atoms (*42*).

The oxidation state of the magnetite surface was found to be dictated by the vacuum-annealing portion of the standard pretreatment sequence. This was verified by XPS analysis of a 300 K surface after vacuum-annealing at successively higher temperatures. Resultant XPS spectra indicated that vacuum-annealing a 300 K surface in steps from 300 to 875 K produced surface states identical to the 300–875 K surfaces created by standard pretreatment.

Auger electron spectroscopy was used to continuously follow the Fe/O ratio of a 300 K surface raised in temperature (heating rate equal to 1 K s^{-1}) under vacuum from 300 to 875 K. The peak-to-peak heights of the Fe(LMM) transition at ca. 700 eV and the O(KLL) transition at ca. 510 eV were monitored with a multiplexer every 10 s. Calculated Fe(LMM)/O(KLL) peak-to-peak height ratios were adjusted to Fe/O atomic ratios by an appropriate factor which gave a final Fe/O atomic ratio of 0.80 (in accordance with XPS results). These AES data along with the XPS ratio data (Scheme B) from Table 2 are plotted in Fig. 5, showing good agreement. A similar AES plot was also obtained by Kelemen *et al.* (*44*) for a vacuum-annealed polycrystalline iron oxide overlayer on Fe(100). They observed that the Fe/O atomic ratio became constant above an annealing temperature of ca. 575–600 K. Using UPS, XPS, and AES, they identified the surface oxide phase in the plateau region as FeO and inferred that

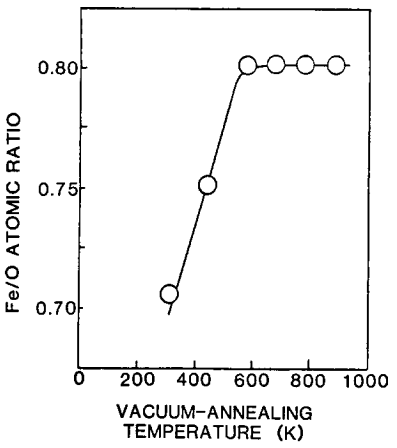

FIG. 5. Fe/O atomic ratios determined for different vacuum-annealing temperatures. The circles denote XPS results and the solid line denotes AES results (see text for explanation).

excess atomic oxygen existed on the surface for lower annealing temperatures (300–500 K).

Finally, XPS experiments studying the effect of vacuum-annealing were performed on a bulk magnetite powder specimen identical to that employed by Lund *et al.* (*30*) for NO adsorption studies. The powder was pressed into a 10 × 10 × 2-mm Cu holder having a slightly indented surface to hold the compressed pellet. XPS spectra were taken of a 300 K surface vacuum-annealed in steps from 300 to 875 K. Results obtained were in good agreement with XPS results from model surfaces. One difference between the two sets of experiments involved the rate of attaining the final state of surface reduction upon vacuum-annealing. The final surface state was reached much more quickly for the nonporous magnetite overlayers on iron than for the porous, high-surface-area magnetite powders (in seconds as opposed to minutes or hours).

DISCUSSION AND SUMMARY

The surface reduction behavior of the magnetite overlayer during vacuum-annealing is illustrated schematically in Fig. 6 for the case of an $Fe_3O_4(100)$ surface. For the 300 K surface, there is a mixture of Fe^{2+}

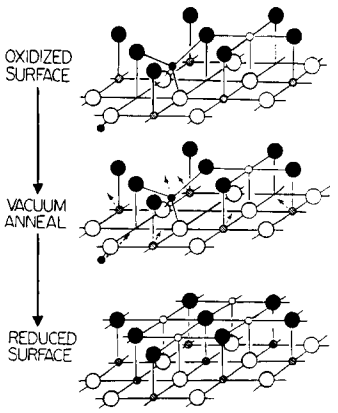

FIG. 6. Schematic representation of surface reduction behavior of the magnetite overlayer during vacuum-annealing. Iron cations are represented by small circles, solid circles for A-sites, open and shaded circles for surface and bulk B-sites, respectively. Oxygen anions are represented by large circles, solid and open circles for surface and bulk anions, respectively.

and Fe^{3+} cations in the surface region. The Fe^{3+} cations are stabilized in full-coordination sites (either fourfold-coordinated, tetrahedral A-sites or sixfold-coordinated, octahedral B-sites). Cations in the immediate surface region are present in lower-coordination sites and cannot exist in the Fe^{3+} state due to the destabilizing effect of the missing oxygen anion neighbors, i.e., these cations are reduced to Fe^{2+} which can better compensate for the missing negatively charged neighbor. Also, Fe^{2+} cations are stabilized in subsurface, fully coordinated B-sites. As the surface is vacuum-annealed at progressively higher temperatures, diffusion of cations toward the surface through the oxygen anion sublattice takes place. Hence, both the surface cation concentration and the degree of surface reduction increase. At the highest annealing temperature of 875 K, a FeO-like surface layer is envisioned with all surface B-sites occupied by Fe^{2+} cations. This surface possesses a net surface ionic charge of zero. Subsequent oxygen treatment of this surface at 300 K adds additional oxygen to the overlayer with diffusion of Fe cations into the oxygen sublattice to create a more-oxidized surface. Vacuum-annealing this surface at 300 K regenerates the 300 K surface state.

It is useful to utilize the Fe/O atomic ratios calculated from XPS spectra to describe more quantitatively the surface composition of the different magnetite surfaces. The inherent uncertainties in these ratios must be noted, however, due to uncertainties in the baseline correction schemes and atomic sensitivity factors employed. The ratios calculated from baseline correction Scheme B are estimated as accurate to within ca. 5–10%. A stoichiometric surface of Fe_3O_4 should show an Fe/O atomic ratio of 0.75 and a Fe^{2+}/Fe^{3+} cation ratio of 0.5. Magnetite surfaces treated at temperatures from 675 to 875 K showed Fe^{2+}/Fe^{3+} ratios near 10 and Fe/O ratios of about 0.89 to 0.80 (according to Schemes A and B, respectively). These surfaces are apparently more like FeO than Fe_3O_4. In contrast, the 300 K surface appears to be more like Fe_3O_4 with more Fe^{3+} cations than Fe^{2+} cations in the analysis volume. This is an indication that the calculated Fe/O value for the 300 K surface of 0.71 is slightly low and a more appropriate value seems to be 0.78, calculated using the linear baseline correction of Scheme A.

Two phenomena are probably responsible for the observation that the reduction of magnetite surfaces by vacuum treatment is more rapid for magnetite overlayers on metallic iron than for high surface area, magnetite powders. First, the porous, high-surface-area nature of the magnetite powder enhances the readsorption rate (of, e.g., desorbed H_2O and O_2) due to locally high partial pressures within the pore structure. This inhibits escape of the desorbed species from the pore structure into the UHV chamber. Due to the nonporous nature of the model magnetite surface, readsorption effects are negligible. Second, the mechanisms of surface reduction are different for the two types of specimens. For magnetite overlayers on metallic iron, surface reduction can occur by interstitial diffusion of Fe cations toward the surface from within the

overlayer since these diffusing cations can be replenished by cations created at the metal–metal oxide interface. For bulk magnetite powders, there is no equivalent source of Fe cations and surface reduction must occur by removal of surface lattice oxygen. It appears that this is a much slower process.

CONCLUSION

A procedure for synthesizing clean magnetite overlayers on iron has been developed. CEMS was utilized to identify that the overlayer was, in fact, Fe_3O_4. It was found that the oxidation state of the surface of this overlayer could be altered by low-pressure oxidation followed by vacuum-annealing at various temperatures, especially below 675 K. These different surfaces were characterized using XPS and AES, which showed that both the degree of surface reduction and the surface cation concentration increased as the vacuum-annealing temperature was increased.

The results of this study provide an experimental strategy for varying the oxidation state of iron oxide surfaces and thereby investigating the effects of surface oxidation state in determining the adsorptive properties of the surface. This is the subject of the following paper (*1*).

Specifically, temperature-programmed desorption studies of O_2, NO, CO_2, and CO will be performed on surfaces vacuum-annealed at various temperatures. In general, adsorbed species which increase in surface coverage with increasing vacuum-annealing temperature can be associated with coordinatively unsaturated iron cations, while adsorbed species which show the opposite trend can be associated with surface oxygen species. In addition to changing the relative numbers of surface sites, it will be shown that varying the surface oxidation state also alters the nature of the adsorbed species.

ACKNOWLEDGMENTS

We are grateful to the National Science Foundation for financial support of this work and for providing a Graduate Fellowship to one of us (TJU). We thank B. Tatarchuk for valuable assistance during the Mössbauer spectroscopy experiments.

REFERENCES

1. Udovic, T. J., and Dumesic, J. A., *J. Catal.* **89,** 314 (1984).
2. Himmel, L., Mehl, R. F., and Birchenall, C. E., *J. Metals* **5,** 827 (1953).
3. Davies, D. E., Evans, U. R., and Agar, J. N., *Proc. Roy. Soc. London, Ser. A* **225,** 29 (1954).
4. Caule, E. J., and Cohen, M., *J. Electrochem. Soc.* **108,** 834 (1961).
5. Hauffe, K., "Oxidation of Metals," p. 267. Plenum, New York, 1965.
6. Boggs, W. E., Kachik, R. H., and Pellissier, G. E., *J. Electrochem. Soc.* **112,** 539 (1965); *114,* 32 (1967).
7. Yolken, H. T., and Kruger, J., *J. Electrochem. Soc.* **114,** 796 (1967).
8. Graham, M. J., and Cohen, M., *J. Electrochem. Soc.* **116,** 1430 (1969).
9. Channing, D. A., and Graham, M. J., *Corros. Sci.* **12,** 271 (1972).
10. Simmons, G. W., Kellerman, E., and Leidheiser, H., Jr., *Corrosion* **29,** 227 (1973).
11. Sewell, P. B., Mitchell, D. F., and Cohen, M., *Surf. Sci.* **33,** 535 (1972).
12. Melmed, A. J., and Carroll, J. J., *J. Vac. Sci. Technol.* **10,** 164 (1973).
13. Leygraf, C., and Ekelund, S., *Surf. Sci.* **40,** 609 (1973).
14. Legg, K. O., Jona, F., Jepsen, D. W., and Marcus, P. M., *Phys. Rev.* **16,** 5271 (1977).
15. Brundle, C. R., *IBM J. Res. Dev.* **22,** 235 (1978).
16. Gebhardt, M., *in* "Crystal Growth: An Introduction" (P. Hartman, Ed.), p. 119. North-Holland, Amsterdam, 1973.
17. Wells, A. F., "Structural Inorganic Chemistry," 4th ed., p. 456. Oxford Univ. Press (Clarendon) Oxford, 1975.
18. Columbo, U., Fagherazzi, G., Gazzarrini, F., Lanzavecchia, G., and Sironi, G., *Nature (London)* **219,** 1036 (1968).
19. Fagherazzi, G., and Lanzavecchia, G., *Mater. Sci. Eng.* **5,** 63 (1969/70).
20. Chen, W. K., and Peterson, N. L., *J. Phys. Chem. Solids* **36,** 1097 (1975).
21. Holt, J. B., and Himmel, L., *J. Electrochem. Soc.* **116,** 1569 (1969).
22. Hagel, W. C., *Trans. Metall. Soc. AIME* **236,** 179 (1966).
23. Goursat, A. G., and Smeltzer, W. W., *Oxid. Met.* **6,** 101 (1973).
24. Sewell, P. B., and Cohen, M., *J. Electrochem. Soc.* **111,** 501, 508 (1964).
25. Wagner, C., *Z. Phys. Chem. B* **21,** 25 (1933).
26. Asami, K., Hashimoto, K., and Shimodaira, S., *Corros. Sci.* **16,** 35 (1976).

27. Hirokawa, K., and Oku, M., *Talanta* **26,** 855 (1979).
28. Rochester, C. H., and Topham, S. A., *J. Chem. Soc. Faraday Trans. 1* **75,** 1073 (1979).
29. Lorenzelli, V., Busca, G., and Sheppard, N., *J. Catal.* **66,** 28 (1980).
30. Lund, C. R. F., Schorfheide, J. J., and Dumesic, J. A., *J. Catal.* **57,** 105 (1979).
31. Tatarchuk, B. J., and Dumesic, J. A., *J. Catal.* **70,** 323 (1981).
32. Sørensen, K., International Report No. 1, Laboratory of Applied Physics II, Technical University of Denmark, Lyngby, Denmark, 1972.
33. McIntyre, N. S., and Zetaruk, D. G., *Anal. Chem.* **49,** 1521 (1977).
34. Barrie, A., and Street, F. J., *J. Electron Spectrosc.* **7,** 1 (1975).
35. Wagner, C. D., Riggs, W. M., Davis, L. E., and Moulder, J. F., *in* "Handbook of X-Ray Photoelectron Spectroscopy" (G. E. Muilenberg, ed.), Perkin–Elmer Corp., Eden Prairie, Minnesota, 1978.
36. Kubsh, J. E., and Dumesic, J. A., *AIChE J.* **28,** 793 (1982).
37. Brucker, C. F., and Rhodin, T. N., *Surf. Sci.* **57,** 523 (1976).
38. Brodén, G., and Bonzel, H. P., *Surf. Sci.* **84,** 106 (1979).
39. Benziger, J., and Madix, R. J., *Surf. Sci.* **94,** 119 (1980).
40. Kubaschewski, O., and Hopkins, B. E., "Oxidation of Metals and Alloys," p. 182. Butterworths, London, 1962.
41. Udovic, T. J., Ph.D. thesis, University of Wisconsin-Madison, 1982.
42. Brundle, C. R., Chuang, T. J., and Wandelt, K., *Surf. Sci.* **68,** 459 (1977).
43. Allen, G. C., Curtis, M. T., Hooper, A. J., and Tucker, P. M., *J. Chem. Soc. Dalton* 1525 (1974).
44. Kelemen, S. R., Kaldor, A., and Dwyer, D. J., *Surf. Sci.* **121,** 45 (1982).